

Available online at www.synsint.com

Synthesis and Sintering

ISSN 2564-0186 (Print), ISSN 2564-0194 (Online)



Research article

A simulative approach to obtain higher temperatures during spark plasma sintering of ZrB_2 ceramics by geometry optimization

Milad Sakkaki ^{ID}^a, Mohsen Naderi ^{ID}^a, Mohammad Vajdi ^{ID}^{a,*},
Farhad Sadegh Moghanlou ^{ID}^{a,*}, Ali Tarlani Beris ^{ID}^b

^a Department of Mechanical Engineering, University of Mohaghegh Ardabili, Ardabil, Iran

^b Department of Mechanical Engineering, College of Engineering, Boston University, Boston, USA

ABSTRACT

This study provides a detailed analysis of the spark plasma sintering (SPS) process for zirconium diboride (ZrB_2) ceramics, utilizing the finite element method in COMSOL Multiphysics. The focus is on understanding the temperature distribution during the SPS of a ZrB_2 sample in a graphite die. Heat diffusion equations, augmented with Joule heating considerations, are utilized to simulate temperature variations within the system over time. Critical boundary conditions at the system's extremities are modeled as convection cooling. The Analysis of Variance (ANOVA) reveals that the diameter of the sample is the most significant factor influencing the peak temperature at the center of the ZrB_2 sample. It is found that the sample diameter's variance accounts for a predominant impact on temperature, markedly more than other factors such as the die's outer diameter and sample thickness. Notably, the standard deviation of the temperature in the axial direction across all samples is less than 4 °C, a value that is statistically minor in comparison to the sintering temperatures, which are around 2000 °C. These findings are instrumental in providing an in-depth understanding of the SPS process, which is essential for the optimization of sintering parameters for ZrB_2 ceramics.

© 2023 The Authors. Published by Synsint Research Group.

KEYWORDS

Zirconium diboride
Numerical analysis
Taguchi method
Temperature distribution
SPS



1. Introduction

Ultra-high-temperature ceramics (UHTCs) represent a recent breakthrough in material science, boasting remarkable properties. These materials exhibit an exceptional temperature tolerance exceeding 3000 °C, outstanding thermal conductivity, and impressive resistance to wear and oxidation [1]. These remarkable features position UHTCs as the perfect candidates for aerospace applications, where they are finding increasing utilization in extreme conditions. This proves invaluable in critical areas such as the leading edges of hypersonic

vehicles, propulsion components, and thermal protection systems. The overall performance of UHTCs relies on their intrinsic properties and the manufacturing methods employed. A crucial determinant of their characteristics is the microstructure of UHTC components; it hinges upon how the ceramic powders are compacted and densified. Various fabrication techniques, from traditional methods like hot pressing (H.P.) to advanced methods like spark plasma sintering (SPS), have been explored to improve the performance of UHTCs [2]. The process of sintering is crucial in creating materials with specific properties. As industries evolve and demand faster and more precise

* Corresponding authors. E-mail address: vajdi@uma.ac.ir (M. Vajdi), f_moghanlou@uma.ac.ir (F. Sadegh Moghanlou)

Received 29 September 2023; Received in revised form 29 November 2023; Accepted 7 December 2023.

Peer review under responsibility of Synsint Research Group. This is an open access article under the CC BY license (<https://creativecommons.org/licenses/by/4.0/>).
<https://doi.org/10.53063/synsint.2023.34178>

methods, spark plasma sintering (SPS) presents an innovative approach to traditional sintering. At its core, SPS is a method that differs in how it heats the material. Instead of relying on external heat sources, common in traditional sintering, SPS uses an electric current to generate heat from within the material itself. This internal heat produced by running electricity through the material, results in faster and often more uniform bonding of particles. One of the main advantages of SPS is its efficiency. Traditional sintering processes can be long, and prolonged exposure to heat can sometimes lead to unwanted changes in the material's structure. In contrast, SPS can achieve the desired results quickly, often at lower temperatures. This makes it especially well-suited for materials that have been difficult to sinter using older methods [3, 4].

To further understand the working mechanism of SPS, it is essential to delve into its unique procedure. Once the material, usually in powder form, is placed inside the SPS device, it is subjected to an electrical and mechanical force. The electrical current, when passed through the powder, creates heat due to the inherent resistance of the particles, leading to what is known as "Joule heating." This heat causes the particles to bond, while at the same time, a mechanical pressure is applied to compact the material. This simultaneous application of heat and pressure ensures a dense, robust final product while maintaining the material's desired properties. The electric pulses, which are short and frequent, contribute to the rapid heating rates, preventing any significant grain growth and resulting in a refined microstructure [5, 6].

Another strength of SPS is the use of numerical methods. These computer techniques provide detailed and nuanced studies of SPS processes and their variables. Through computational modeling, one can obtain clear and comprehensive information about the sintering process and the transformations that materials undergo during it. This information may not be as easily or precisely derived from experimental methods alone. Numerical approaches have several advantages over experimental ones, including the ability to analyze more data, lower costs and time, and higher precision results. As a result, numerical simulations and modeling have become increasingly common in SPS research. Undoubtedly, as we progress, these computational methods will play an even more significant role in advancing this technology [7, 8].

Understanding temperature distributions, densification behaviors, and electrical nuances is crucial in the domain of spark plasma sintering (SPS) and Field Activated Sintering (FAST) processes. Multiple researchers have investigated these parameters to enhance the optimization and control of these methods [9].

Yucheng and Zhengyi [10] tackled the SPS process, underlining inherent temperature disparities in samples. For electrically conductive specimens, they demonstrated that modulating power during temperature elevation could shift this gradient. Diving deeper into temperature variations, Shen et al. [11] focused on SPS parameters for sub-micrometer-sized Al_2O_3 powder, noting an early densification attributed to spark-discharge processes. Their work also highlighted the significance of temperature in determining grain-boundary diffusion and migration.

Further exploring temperature dynamics, Matsugi et al. [12] conducted a pivotal study on voltage and temperature distribution during spark sintering. Using both titanium and alumina powders, they observed distinct temperature distribution differences. Their results, grounded in Ohm's and Fourier's laws, presented a methodology for estimating

voltage and temperature distributions, irrespective of the system's makeup.

Supplementing the understanding of temperature distribution, Guo et al. research [13] on ZrB_2 ceramics in SPS indicated the process's efficiency in achieving densification. Their findings accentuated the determinative role of sintering temperature, heating rate, and holding time. Meanwhile, Pavia's group [14] embarked on deciphering the SPS process's critical parameters, emphasizing the role of Joule heating. They effectively refined an electro-thermal numerical model, spotlighting the importance of electrical resistivity and thermal conductivity.

Grasso's team [15] probed deeper into the SPS setup, investigating the relationship between applied pressures and temperature distribution. Their combined experimental and computational approach elucidated the effects of punch's Poisson deformation on temperature gradients. In a complementary study, Vanmeensel and collaborators [16] offered insights into the FAST process. Their analysis between electrical conductors and insulators unveiled nuances in temperature gradients but maintained measurement accuracy.

The primary goal of thermal modeling in the SPS process is to modify the temperature distribution within the sample and the entire system, enabling optimized control over the process and the eventual microstructure of the products. Recognizing the prominence of the SPS process in producing UHTCs, this study delves into the numerical investigation of temperature distribution during the spark plasma sintering of ZrB_2 ceramics. Zirconium diboride (ZrB_2), a UHTC, has garnered significant interest due to its exceptionally high melting point, low density, and other notable properties like chemical inertness against molten metals and impressive thermal shock resistance [17]. The temperature gradients established during sintering directly influence the resultant microstructure and, by extension, the mechanical characteristics of the product. Hence, the findings from this study provide a granular understanding of temperature variations at every stage. The computational domain employed the finite element method (FEM) to solve the coupled physics intrinsic to the sintering process, specifically the thermo-electric coupling. To enhance the depth of this research, a Taguchi method and a Sensitivity analysis were integrated, focusing on variations in die and sample diameter as well as the sample's height, further refining the understanding of temperature distribution impacts.

2. Methodology

2.1. Design of experiments

To research sintering processes, especially spark plasma annealing, there are many parameters to study, the most important of which are the sintering temperature, holding time, and applied pressure [18–21]. Apart from these main parameters, other items can be added to this list, including the sintering furnace atmosphere, heating rate, cooling rate, and the type and amount of different additives to the powder of the main material [22, 23]. Examining these parameters at different levels requires a vast amount of experiments, which, in practice, requires spending a lot of time, money, and energy. Therefore, it seems that determining the optimal conditions with different parameters and levels is not easy if all those tests are to be carried out.

There are ways to overcome the abovementioned problem and suggestions for doing fewer experiments as an anthology, including the

Taguchi method. This methodology minimizes the number of tests required to determine the optimal state using orthogonal arrays. The Taguchi method combined with the analysis of variance (ANOVA) enables the researcher to assess the significance of all input parameters on the desired output parameter and to obtain the contribution of these parameters in the optimal state. In addition, the Taguchi model can also predict the result of the output parameter in the optimal state. Generally, the quality characteristics are divided into three classes in this method: "nominal is better", "smaller is better", or "greater is better" [24].

The goal of this numerical work is to study the spark plasma sintering of ZrB₂ samples and optimize three geometric parameters to maximize the achievable temperature in the sample center. To design numerical runs and perform statistical evaluations, Qualitek-4 software is employed. The graphite die outer diameter, the sintered sample diameter that is equal to the die inner diameter, and the sintered sample thickness are investigated as the input parameters. In fact, a greater temperature with minimal deviations of temperature in radial and axial directions is desired. Therefore, the qualitative characteristics are chosen according to Table 1.

Although theoretically, any level can be determined for each parameter, and logically, it is better to choose reasonable levels based on previous studies. Therefore, the levels suggested in Table 2 are selected for the input parameters in this research. Since three input parameters are considered in three levels, the Taguchi model suggests the use of L9 orthogonal arrays. The advantage of this proposal is that it reduces the number of required runs from 27 to 9. Of course, in the end, a new run is also performed to compare and validate the predicted value in optimal conditions.

2.2. Geometry

In this research, the chosen geometric setup includes two graphite punches, a graphite die encompassing the specimen, conical spacers, and water-cooled electrodes, as outlined in the reference [25]. The detailed architecture and dimensions of the specimen/die configuration are exhibited in Fig 1. The dimensions of essential variable parameters, as presented in Fig. 1, are enumerated in Table 3. Furthermore, other geometric dimensions are parametrically denoted by the variable L, providing an in-depth representation of the system's structure.

2.3. Governing equations and the numerical procedure

In the spark plasma sintering (SPS) process, heat generation occurs due to the Joule heating effect as an electric current traverses the material. This heat arises from intermolecular frictions and vibrations induced by the flow of electrons. To accurately model this phenomenon, it is essential to determine the electric current distribution within the material. Subsequently, to calculate the temperature at each point within the material, two sets of governing equations must be solved:

Table 1. Investigated output parameters and appropriate quality characteristics.

Output studied parameter	Quality characteristic
Sample center temperature	Greater is better
Temperature standard deviation	Smaller is better

Table 2. Investigated parameters and considered levels.

Parameter	Level 1	Level 2	Level 3
Die outer diameter (cm)	6	8	10
Sample diameter (cm)	2.5	3.5	4.5
Sample thickness (cm)	0.3	0.6	0.9

the electric charge conservation and the energy conservation equations. The governing equation for the flow of direct current (DC) in the material is derived from Maxwell's equations and is represented as Eq. 1 [26]:

$$\nabla J = \nabla(\sigma E) = \nabla(-\sigma \nabla U) = 0 \quad (1)$$

In this equation, J , E , V , and σ denote the current density, the electric field, the electric potential, and the material's electrical conductivity, respectively.

Given that the geometry of the material in the spark plasma sintering (SPS) process is cylindrical, it is more appropriate to employ the axisymmetric form of the governing equations. The energy conservation equation, adapted for cylindrical coordinates, is presented as Eq. 2:

$$\rho C_p \frac{\partial T}{\partial t} = \frac{1}{r} \frac{\partial}{\partial r} (rk_r \frac{\partial T}{\partial r}) + \frac{1}{z} \frac{\partial}{\partial z} (rk_z \frac{\partial T}{\partial z}) + q_i \quad (2)$$

In this equation k_r and k_z represent the thermal conductivity in the radial (r) and axial (z) directions, respectively. ρ denotes the material density, C_p is the heat capacity, and T signifies the temperature. The term q_i in Eq. 2 accounts for the heat generated per unit volume per unit time due to Joule heating. This heat generation term is further defined by Eq. 3:

$$q_i = JE \quad (3)$$

here, E stands for the electric field.

Eq. 4 is the governing equation for electric current in the cylindrical coordinate system:

$$\frac{1}{r} \frac{\partial (ri_r)}{\partial r} + \frac{\partial i_z}{\partial z} = 0 \quad (4)$$

Table 3. Designed numerical runs based on an L9 orthogonal array.

Run No.	Die outer diameter (D ₂)	Sample diameter (D ₁)	Sample thickness (z)
1	6	2.5	0.3
2	6	3.5	0.6
3	6	4.5	0.9
4	8	2.5	0.6
5	8	3.5	0.9
6	8	4.5	0.3
7	10	2.5	0.9
8	10	3.5	0.3
9	10	4.5	0.6

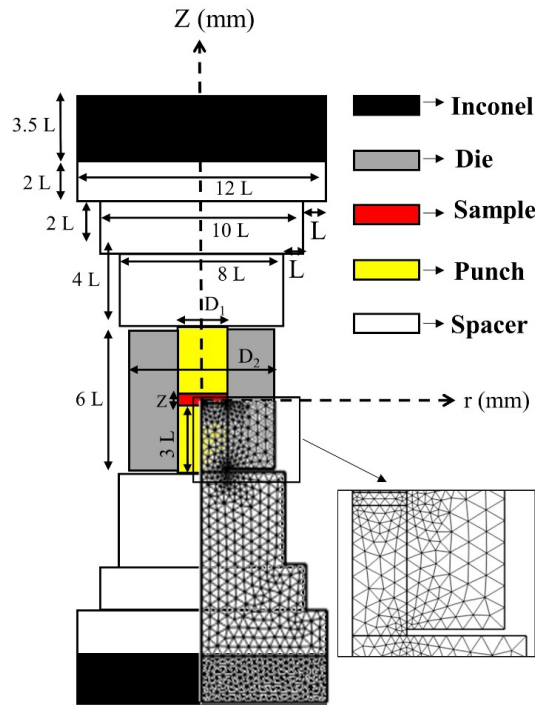


Fig. 1. Detailed architectural and dimensional representation of the SPS setup featuring an illustrative mesh.

In this equation, i_r and i_z denote the current density in the radial (r) and axial (z) directions, respectively. It is noteworthy to express that the spark plasma sintering (SPS) apparatus generates a pulsatile current. To assess the power dissipated in the heating tools, it is crucial to determine the Root-Mean-Square (RMS) values for both the voltage and the current intensity.

The RMS value of the voltage is calculated using Eq. 5 [16]:

$$U_{\text{RMS}} = \sqrt{\frac{1}{P} \int_{t-T}^t u^2(\tau) d\tau} \quad (5)$$

Here, u represents the instantaneous voltage applied to the sample, and T is the period of the alternating current (AC). A similar expression is used to calculate the RMS intensity of the current.

2.4. Material properties

In thermoelectric analyses, there is a strong coupling between electrical

and thermal properties. Given the significant temperature variations encountered during the sintering process, it is imperative to treat material properties as temperature-dependent variables. A comprehensive list of these properties, as a function of temperature, is provided in Table 4.

2.5. Boundary and initial conditions

The spark plasma sintering (SPS) apparatus is initially assumed to have a uniform temperature of 300 K. The voltage applied is time-dependent, and the electric potential at both electrodes is set to zero initially. To adequately solve Eq. 3 and 4, appropriate electrical and thermal boundary conditions must be established. These conditions are illustrated in Fig. 2.

All sides of the equipment are assumed to be electrically insulated. An effective voltage is applied to the upper horizontal surface, while the electric potential at the lower horizontal surface is set to zero (refer to

Table 4. Temperature-dependent properties of graphite, ZrB_2 , and Al_2O_3 (temperature in Kelvin, T).

Material	Inconel [14]	Graphite [14]	ZrB_2	Al_2O_3 [14]
Heat capacity (J/Kg k)	$344 + 0.25 \times T$	$34.27 + 2.72 \times T - 9.6 \times 10^{-4} \times T^2$	$0.704 + 2.52 \times 10^{-5} \times T - 80.2 \times T^{-1}$ [14]	850
Density (Kg/m^3)	8430	$1904 - 0.01414 \times T$	6080 [27]	3899
Thermal conductivity (W/m k)	$10.09 + 0.0157 \times T$	$82.85 - 0.06 \times T + 2.58 \times 10^{-5} \times T^2$	$60.316 + 0.0041 \times T$ [27]	$39500 \times T^{-1.26}$
Electric resistivity (Ωm)	$9.82 \times 10^{-7} + 1.6 \times 10^{-10} \times T$	$2.14 \times 10^{-5} - 1.34 \times 10^{-8} \times T + 4.42 \times 10^{-12} \times T^2$	$0.0589 \times T + 5.4894 \times 10^{-8}$ [27]	$8.7 \times 10^9 \times T^{-4.82}$

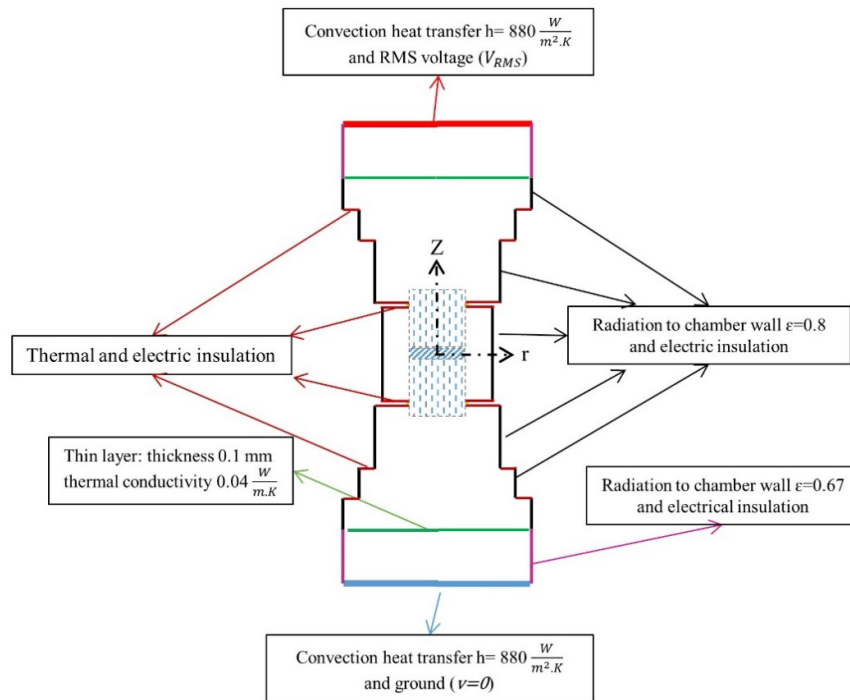


Fig. 2. Detailed overview of the boundary conditions.

Fig. 2). Heat removal by water-cooling at the ramps necessitates the use of a convective heat transfer boundary condition across both the upper and lower horizontal surfaces, as described by Eq. 6:

$$q_c = h_c(T_s - T_w) \quad (6)$$

Eq. 6, q_c denotes the convective heat flux, while h_c , T_s , and T_w represent the convective heat transfer coefficient, the horizontal surface temperature, and the water temperature, respectively. A specific value of $h_c = 880 \text{ (W/m}^2\cdot\text{K)}$ [25] is applied to both the upper and lower surfaces for the convective heat transfer coefficient. As the entire apparatus is situated in a vacuum chamber, convective heat loss from the lateral surfaces is considered negligible. Instead, heat loss is assumed to occur solely through radiation, as described by the Stefan-Boltzmann law in Eq. 7:

$$q_r = \sigma_s \cdot \epsilon \cdot (T_e^4 - T_a^4) \quad (7)$$

In this equation, q_r signifies the radiation heat flux, σ_s is the Stefan-Boltzmann constant, and ϵ denotes the material's emissivity, which is assumed to be 0.8 for graphite [28] and 0.67 for Inconel [29]. T_e represents the emission surface temperature, specifically the surface temperature of the graphite die and punch, while T_a is the temperature of the chamber wall.

A thorough depiction of the boundary conditions is provided in Fig. 2, where the interface between the Inconel and the spacer, highlighted by green lines, plays a crucial role in heat exchange. This interface is conceptualized as a thin layer, measuring 0.1 mm in thickness and exhibiting a thermal conductivity of $0.04 \text{ W/m}^2\cdot\text{K}$, as noted in reference [30]. Additionally, the Electrical Contact Resistance (ECR) is not considered significant at this interface, owing to its extensive area and minimal heat dissipation, as described in the same reference.

Previous experimental work by Manière et al. [30] has shown that ECR decreases with increasing temperature and applied pressure. In the current study, where pressures and temperatures are on the order of 100 MPa and 2000 °C, respectively, ECR can be considered negligible [14]. Therefore, the remaining interfaces, subjected to these high pressures and temperatures, are assumed to be continuous in terms of their thermal and electrical conductivities, as per Pavia et al. [14]. In the numerical analysis, mesh independence was verified by evaluating various mesh configurations with differing sizes and shapes. The final selection was a mesh composed of 1738 elements, which met the requirements for mesh independence. A representative illustration of this meshed geometry is shown in Fig. 1. Due to the high current density observed in the sample and the surrounding die, a finer mesh was utilized in these areas to capture the detailed behavior more precisely.

3. Results and discussion

Validating the accuracy of numerical simulation outcomes is a crucial step. To achieve this, the results from the current simulation were compared with the experimental findings of Pavia et al. [14], who conducted sintering studies on Al_2O_3 . This validation exercise was conducted under identical conditions, focusing on temperatures at coordinates $(r,z) = (18,0)$. Fig. 3 presents both the simulation results and the experimental data for these temperature points, demonstrating a close alignment between the two. The congruence observed in Fig. 3 lends credibility to the numerical method used, suggesting its applicability for simulating the sintering process of ZrB_2 samples. Being sure of the accuracy of the employed numerical method, all nine runs, shown in Table 3, were simulated through COMSOL

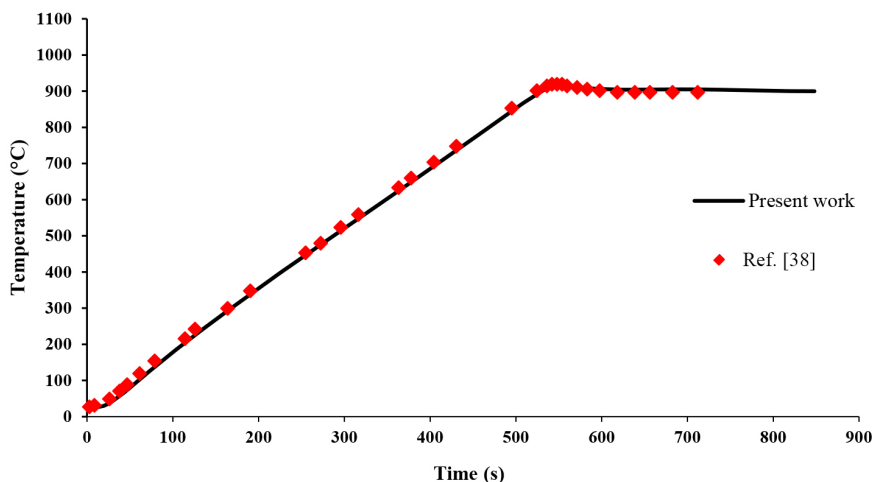


Fig. 3. Comparison between simulated and experimental temperature data at coordinates (r,z)=(18,0).

Multiphysics. With the aim of checking the maximum temperature at the center of the sample and the uniformity of the temperature distribution, temperature contours for runs No. 1 and No. 9 are shown in Fig. 4 to Fig. 7 for the sample and the whole sample-die-punch assembly.

Based on the temperature contours in Fig. 5 and Fig. 7, it can be concluded that the temperature uniformity in the axial direction is completely achieved, and slight variance is expected. On the other hand, the radial temperature distribution is not uniform in these two runs, shown in Fig. 4 and Fig. 6, which can result in a non-uniform structure in the as-sintered sample.

The results obtained from the simulation and numerical analysis on the ZrB₂ ceramics during the spark plasma sintering about the maximum temperature of the center of the samples are presented in Table 5. Also, the standard deviation values of temperature in radial and axial directions are reported in this table. The maximum temperatures calculated for the center of the samples fluctuate from 1791.0 °C in run

No. 7 to 2075.3 °C for run No. 6. It should be noted that the simulation of all ZrB₂ samples is done assuming the same electric current in all of them. According to statistical calculations, the ground average of the maximum temperature of the center of nine samples is 1945.7 °C with a standard deviation of 103.4 °C. There is a difference of 284.3 °C between the highest and lowest temperatures reported in Table 5, which is very effective in the sintering of ZrB₂ and will definitely lead to different results regarding the densification of this ceramic. In other words, at lower temperatures, it is not possible to make a dense ceramic, but at higher temperatures, the amount of porosity decreases, and the chance of obtaining a fully dense specimen increases [31, 32]. Of course, other parameters are also effective in the sintering of ceramics, such as applied pressure and holding time at the maximum temperature, as well as the addition of additives and sintering aids [33, 34]. It is also worth mentioning that the dominant densification

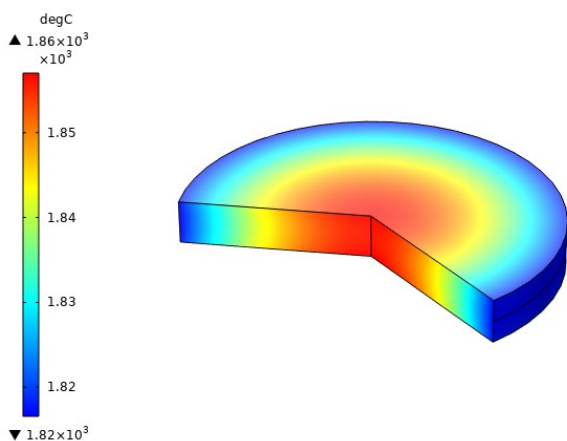


Fig. 4. Temperature contour of the sample for run No. 1.

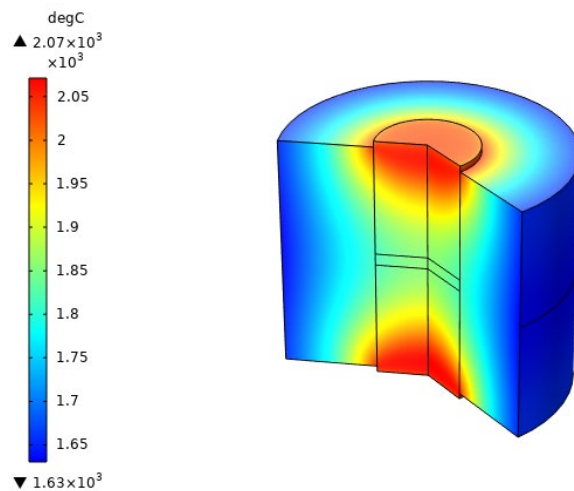


Fig. 5. Temperature contour of the whole sample-die-punch assembly for run No. 1.

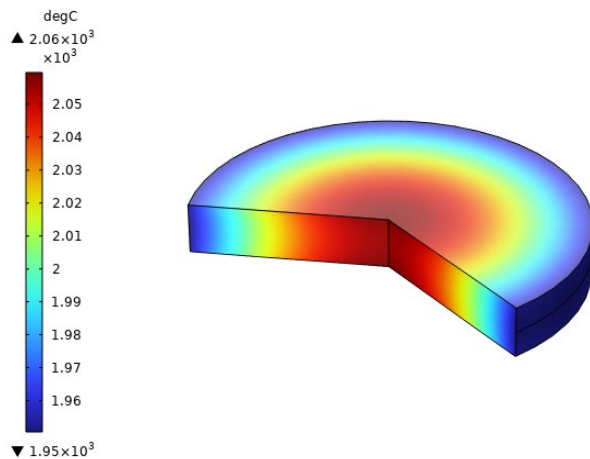


Fig. 6. Temperature contour of the sample for run No. 9.

mechanisms detected in the ZrB_2 -based ceramics change at different temperatures. For example, diffusion prevails at high temperatures, plastic deformation dominances at intermediate temperatures, and particle defragmentation and rearrangement occur at lower temperatures [35, 36].

The standard deviation of the temperature in the axial direction in all samples is very small and below 4 °C. Such a value, compared to the investigated sintering temperatures of ~2000 °C, is not only insignificant from a statistical viewpoint but also negligible from an engineering approach. Although the standard deviation of the temperature in the radial direction cannot be ignored, these values are not giant enough to overshadow the statistical comparisons. Anyway, the highest and the lowest standard deviations for the temperature in the radial direction are observed in runs No. 5 and No. 2, respectively. Fig. 8 shows the main effect bar charts of the average values for the ZrB_2 sample center temperature. The mean temperature of the sample center slightly drops from 1954.8 °C to 1948.1 °C and then to 1934.3 °C with the increase of the die outer diameter from 6 cm to

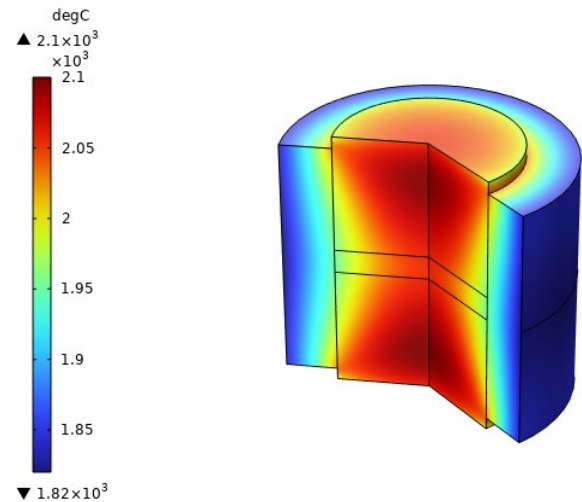


Fig. 7. Temperature contour of the whole sample-die-punch assembly for run No. 9.

8 cm and then to 10 cm. Although there is a greater temperature drop in the second step than in the first step, in general, not much change is seen due to the increase in die outer diameter. Contrary to the insignificant effect of the die outer diameter on the average temperature, if the sample diameter increases from 2.5 cm to 3.5 cm, a very sharp increase in the mean temperature is seen as it enhances from 1822.6 °C to 1958.6 °C. It is really interesting to observe that only by increasing the radius of the ZrB_2 sample by 0.5 cm, such a jump of 136 °C in the average temperature of the sample center is created. Another interesting point is that as the sample diameter increases from 3.5 cm to 4.5 cm, a further increase (about 100 °C) is observed in the average temperature up to 2056.0 °C. Totally, if the radius of the sample increases by only 1 cm, the average temperature shows a surprising increase of more than 230 °C, which is very remarkable in the sintering of ceramics. It is worth reminding that the sample

Table 5. Simulation results of the ZrB_2 sample center temperature.

Run No.	Sample center temperature (°C)	Temperature standard deviation in radial direction (°C)	Temperature standard deviation in axial direction (°C)
1	1855.7	49.3	0.4
2	1971.9	23.5	1.6
3	2036.8	56.0	3.0
4	1821.1	63.9	1.7
5	1948.0	70.6	3.6
6	2075.3	64.8	0.3
7	1791.0	65.1	3.7
8	1955.8	61.7	0.4
9	2056.0	67.8	1.3
Grand average	1945.7		
Standard deviation	103.4		

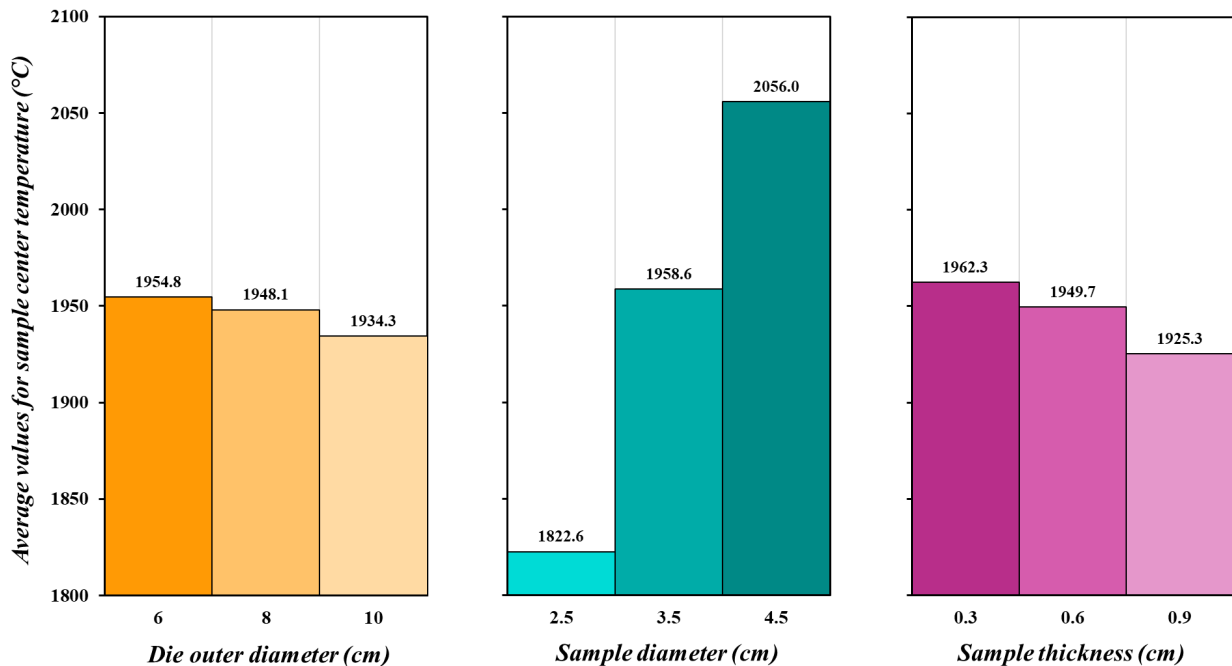


Fig. 8. Main effect bar charts of the average values for the ZrB_2 sample center temperature.

diameter is the same as the die's inner diameter. Therefore, it is surprising that during the sintering of ZrB_2 inside a graphite die, the average temperature in the sample center is strongly affected by the die's inner diameter. Still, it is indifferent to its outer diameter. In examining the effect of sample thickness on the average temperature, it is seen that the trend, both qualitatively and quantitatively, is more or less similar to the effect of the die outer diameter. By increasing the sample thickness from 0.3 cm to 0.6 cm and then to 0.9 cm, the mean temperature slightly drops from 1962.3 °C to 1949.7 °C and then 1925.3 °C. With the general comparison of all three geometric input parameters, it seems that the sample diameter has a stronger effect on the average temperature than other parameters.

The ANOVA data of the investigated parameters on the center temperature of the ZrB_2 sample are presented in Table 6. Several statistical computations are reported in this table, among which the degree of freedom can be mentioned, but the most important is the significance column. In fact, this column shows the percentage of influence and importance of each of the input parameters under investigation on the desired output parameter(s). Therefore, based on the statistical findings as could be expected, the sample diameter with a remarkable significance of ~96% shows the greatest effect on the

maximum temperature of the ZrB_2 sample center in comparison with other investigated parameters. The sample thickness is second in importance, which is ~2%, and in the comparison of the sample diameter, its effect can be almost ignored. The significance of the die outer diameter is below 1%, and it is not very important among the investigated geometrical parameters. According to ANOVA, the significance of errors or other parameters that have not been checked is around 2%. Therefore, it is interesting that this item is as important as the sample thickness, and even compared to the die outer diameter, it seems to be more effective on the center temperature of sintering ZrB_2 ceramics.

By drawing a pie chart for the above-discussed items, as shown in Fig. 9, an easier and better visual understanding of the effect of the input parameters on the output parameter can be obtained. This diagram clearly shows that the sample diameter is the most important parameter that must be considered to achieve the maximum temperature in the center of ZrB_2 ceramic, so even the sample thickness and the die outer diameter can be ignored. In other words, there is no need to control these insignificant parameters as their significance is almost equal and even less than that of the evaluated error value in statistical investigations. Of course, it should be emphasized that these

Table 6. ANOVA results of the investigated parameters on the ZrB_2 sample center temperature.

Parameter	Degrees of freedom	Sum of squares	Variance	F-ratio	Pure sum	Significance (%)
Die outer diameter	2	660.261	330.130	1.877	308.598	0.360
Sample diameter	2	82479.808	41239.904	234.542	82128.145	95.930
Sample thickness	2	2120.745	1060.372	6.030	1769.082	2.066
Other/Error	2	351.662	175.831	-	-	1.644
Total	8	85612.478	-	-	-	100.000

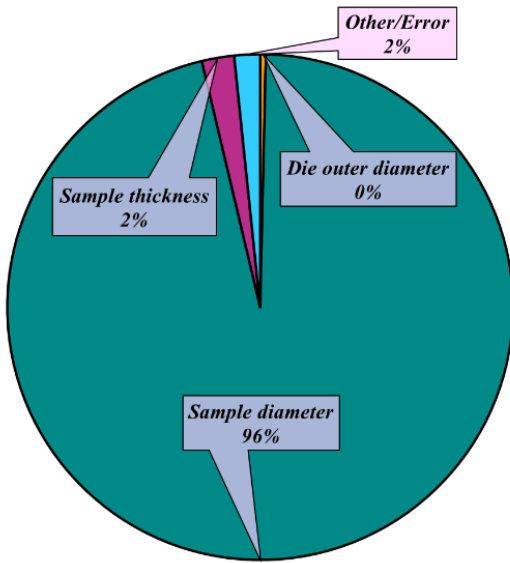


Fig. 9. Pie chart of significance of the investigated parameters on the ZrB₂ sample center temperature.

comparisons and reported values are only true for the chosen levels of each parameter. If other levels are considered for input parameters, new results will be obtained that may be similar or different from the current findings. The most important point obtained from this research is that in designing a graphite die for spark plasma sintering of ZrB₂ ceramics, its inner diameter is much more important than its outer diameter. That is, if technical considerations allow, in order to save the amount of graphite material used and reduce the costs, it is better to consider the minimum wall thickness for the cylindrical graphite die.

Table 7 summarizes the statistical calculations to determine the optimal simulation conditions in order to achieve the highest temperature in the center of the ZrB₂ sample, which is based on the contribution of each of the input parameters to the output result. According to this table, by choosing 6 cm as the die outer diameter, which is level 1 of this parameter, a contribution of 1.9 °C can be expected. By selecting the third level for the sample diameter, which is 4.5 cm, a significant contribution of 110.3 °C is obtained. In addition to these, considering the sample thickness in level 1 as 0.3 cm provides a contribution of 16.5 °C. These values show the individual contribution of each of the parameters in the optimal state, and their sum which is called the total

Table 7. Contributions of the input parameters on the ZrB₂ sample center temperature in an optimal state.

Parameter	Level	Level description	Contribution (°C)
Die outer diameter	1	6 cm	9.1
Sample diameter	3	4.5 cm	110.3
Sample thickness	1	0.3 cm	16.5
Total contributions			135.9
Grand average			1945.7
Temperature expected in optimal state			2081.6

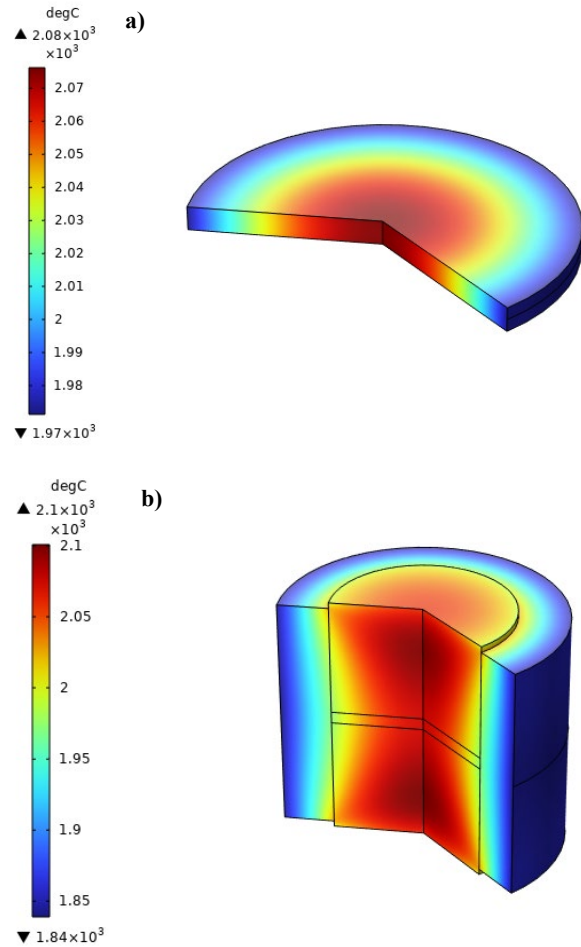


Fig. 10. Temperature contours of a) the sample and b) the whole assembly for the optimal conditions.

contributions is 135.9 °C. The grand average maximum temperature of the sample center for 9 simulated runs is already found to be 1945.7 °C, as reported in Table 5. If this grand average value is added to the current calculated total contributions, a maximum temperature of 2081.6 °C is predicted in the optimal state.

At the end, a new run is performed as the verification step using Comsol Multiphysics software to compare the accuracy of this predicted value with the numerically achieved value in the optimal state. Logically, except for the geometric input parameter, the rest of the simulation conditions will be the same as the previous nine runs. By doing this, i.e., performing a new run in optimal conditions where the die outer diameter is 6 cm, the sample thickness is 0.3 cm, and the sample diameter is 4.5 cm, a maximum temperature of 2075.3 °C is numerically obtained for the center of the ZrB₂ ceramic. The temperature contours for the sample and the sample-die-punch geometry for this optimal run are illustrated in Fig. 10. As seen, this numerically-achieved value in optimal conditions is very close to the one predicted by Taguchi method (2081.6 °C) and has a slight difference of 6.3 °C. Since this difference is insignificant compared to the sintering temperature itself (~2000 °C), the results of the Taguchi model can be declared valid in this numerical analysis.

4. Conclusions

This study embarked on an in-depth thermal analysis of the spark plasma sintering (SPS) process for zirconium diboride (ZrB_2) ceramics using COMSOL Multiphysics and the finite element method. The key findings are:

- **Temperature Distribution and Influencing Factors:** The temperature distribution within the ZrB_2 sample was critically dependent on specific geometric parameters, particularly the sample diameter. This parameter was found to be the most significant in influencing the maximum temperature at the center of the sample.
- **Statistical Significance:** Statistical analyses, including ANOVA, underscored the predominance of the sample diameter over other factors like the die's outer diameter and sample thickness in affecting the temperature profile.
- **Implications for Sintering Process:** The variation in temperatures, which was within a narrow standard deviation, signifies a consistent and controlled sintering process, essential for achieving desired material properties.
- **Engineering Insights:** The minimal variation in temperature, especially in the axial direction of the samples, demonstrates the precision and effectiveness of the SPS process, making it a viable method for producing high-quality ZrB_2 ceramics.

CRedit authorship contribution statement

Milad Sakkaki: Data curation.

Mohsen Naderi: Software, Writing – original draft.

Mohammad Vajdi: Conceptualization, Supervision, Writing – review & editing.

Farhad Sadegh Moghanlou: Project administration, Supervision, Writing – review & editing.

Ali Tarlani Beris: Validation, Software.

Data availability

The data underlying this article will be shared on reasonable request to the corresponding author.

Declaration of competing interest

The authors declare no competing interests.

Funding and acknowledgment

The authors gratefully acknowledge the University of Mohaghegh Ardabili for the support of this research. The resources provided by Boston University have been pivotal in the realization of this work. These supports have significantly contributed to the successful completion of this study and are deeply acknowledged by the authors.

References

- [1] S.K. Thimmappa, B.R. Golla, V.V. Bhanu Prasad, Oxidation behavior of silicon-based ceramics reinforced diboride UHTC: a review, *Silicon*. 14 (2022) 12049–12074. <https://doi.org/10.1007/s12633-022-01945-8>.
- [2] A.S. Mukasyan, A.S. Rogachev, D.O. Moskovskikh, Z.S. Yermekova, Reactive spark plasma sintering of exothermic systems: A critical review, *Ceram. Int.* 48 (2022) 2988–2998. <https://doi.org/10.1016/j.ceramint.2021.10.207>.
- [3] P. Cavaliere, B. Sadeghi, A. Shabani, Spark plasma sintering: process fundamentals, in: *Spark Plasma Sinter. Mater.*, Springer International Publishing, Cham. (2019) 3–20. https://doi.org/10.1007/978-3-030-05327-7_1.
- [4] Z.-Y. Hu, Z.-H. Zhang, X.-W. Cheng, F.-C. Wang, Y.-F. Zhang, S.-L. Li, A review of multi-physical fields induced phenomena and effects in spark plasma sintering: Fundamentals and applications, *Mater. Des.* 191 (2020) 108662. <https://doi.org/10.1016/j.matdes.2020.108662>.
- [5] E. Ranjbarpour Niari, M. Vajdi, M. Sakkaki, S. Azizi, F. Sadegh Moghanlou, M. Shahedi Asl, Finite element simulation of disk-shaped HfB₂ ceramics during spark plasma sintering process, *Int. J. Appl. Ceram. Technol.* 19 (2022) 344–357. <https://doi.org/10.1111/ijac.13886>.
- [6] D. Bubesh Kumar, B. Selva babu, K.M. Aravind Jerrin, N. Joseph, A. Jiss, Review of spark plasma sintering process, *IOP Conf. Ser. Mater. Sci. Eng.* 993 (2020) 012004. <https://doi.org/10.1088/1757-899X/993/1/012004>.
- [7] F. Sadegh Moghanlou, M. Vajdi, M. Sakkaki, S. Azizi, Effect of graphite die geometry on energy consumption during spark plasma sintering of zirconium diboride, *Synth. Sinter.* 1 (2021) 54–61. <https://doi.org/10.53063/synsint.2021.117>.
- [8] M. Vajdi, F. Sadegh Moghanlou, Z. Ahmadi, A. Motallebzadeh, M. Shahedi Asl, Thermal diffusivity and microstructure of spark plasma sintered TiB₂-SiC-Ti composite, *Ceram. Int.* 45 (2019) 8333–8344. <https://doi.org/10.1016/j.ceramint.2019.01.141>.
- [9] Y. Le Godec, S. Le Floch, Recent developments of high-pressure spark plasma sintering: an overview of current applications, challenges and future directions, *Materials (Basel)*. 16 (2023) 997. <https://doi.org/10.3390/ma16030997>.
- [10] W. Yucheng, F. Zhengyi, Study of temperature field in spark plasma sintering, *Mater. Sci. Eng. B*. 90 (2002) 34–37. [https://doi.org/10.1016/S0921-5107\(01\)00780-2](https://doi.org/10.1016/S0921-5107(01)00780-2).
- [11] Z. Shen, M. Johnsson, Z. Zhao, M. Nygren, Spark plasma sintering of alumina, *J. Am. Ceram. Soc.* 85 (2002) 1921–1927. <https://doi.org/10.1111/j.1151-2916.2002.tb00381.x>.
- [12] K. Matsugi, H. Kuramoto, T. Hatayama, O. Yanagisawa, Temperature distribution at steady state under constant current discharge in spark sintering process of Ti and Al₂O₃ powders, *J. Mater. Process. Technol.* 134 (2003) 225–232. [https://doi.org/10.1016/S0924-0136\(02\)01039-7](https://doi.org/10.1016/S0924-0136(02)01039-7).
- [13] S. Guo, T. Nishimura, Y. Kagawa, J. Yang, Spark plasma sintering of zirconium diborides, *J. Am. Ceram. Soc.* 91 (2008) 2848–2855. <https://doi.org/10.1111/j.1551-2916.2008.02587.x>.
- [14] A. Pavia, L. Durand, F. Ajustron, V. Bley, G. Chevallier, et al., Electro-thermal measurements and finite element method simulations of a spark plasma sintering device, *J. Mater. Process. Technol.* 213 (2013) 1327–1336. <https://doi.org/10.1016/j.jmatprotec.2013.02.003>.
- [15] S. Grasso, Y. Sakka, G. Maizza, Pressure effects on temperature distribution during spark plasma sintering with graphite sample, *Mater. Trans.* 50 (2009) 2111–2114. <https://doi.org/10.2320/matertrans.M2009148>.
- [16] K. Vanmeensel, A. Laptev, J. Hennicke, J. Vleugels, O. Vanderbiest, Modelling of the temperature distribution during field assisted sintering, *Acta Mater.* 53 (2005) 4379–4388. <https://doi.org/10.1016/j.actamat.2005.05.042>.
- [17] M. Naderi, M. Vajdi, F. Sadegh Moghanlou, H. Nami, Sensitivity analysis of fluid flow parameters on the performance of fully dense ZrB₂-made micro heat exchangers, *Synth. Sinter.* 3 (2023) 88–106. <https://doi.org/10.53063/synsint.2023.32143>.
- [18] M. Stuer, P. Bowen, Z. Zhao, Spark plasma sintering of ceramics: from modeling to practice, *Ceramics*. 3 (2020) 476–493. <https://doi.org/10.3390/ceramics3040039>.

- [19] M. Sakkaki, S.M. Arab, In-situ synthesized phases during the spark plasma sintering of g-C₃N₄ added TiB₂ ceramics: A thermodynamic approach, *Synth. Sinter.* 3 (2023) 73–78. <https://doi.org/10.53063/synsint.2023.32151>.
- [20] P.M. Radingoana, S. Guillemet-Fritsch, P.A. Olubambi, G. Chevallier, C. Estournès, Influence of processing parameters on the densification and the microstructure of pure zinc oxide ceramics prepared by spark plasma sintering, *Ceram. Int.* 45 (2019) 10035–10043. <https://doi.org/10.1016/j.ceramint.2019.02.048>.
- [21] E. De Bona, L. Balice, L. Cognini, M. Holzhäuser, K. Popa, O. Walter, M. Cologna, D. Prieur, T. Wiss, G. Baldinozzi, Single-step, high pressure, and two-step spark plasma sintering of UO₂ nanopowders, *J. Eur. Ceram. Soc.* 41 (2021) 3655–3663. <https://doi.org/10.1016/j.jeurceramsoc.2021.01.020>.
- [22] M. Shirani, M. Rahimpour, M. Zakeri, S. Safi, T. Ebadzadeh, ZrB₂-SiC-WC coating with SiC diffusion bond coat on graphite by spark plasma sintering process, *Ceram. Int.* 43 (2017) 14517–14520. <https://doi.org/10.1016/j.ceramint.2017.07.123>.
- [23] P. Sengupta, S.S. Sahoo, A. Bhattacharjee, S. Basu, I. Manna, Effect of TiC addition on structure and properties of spark plasma sintered ZrB₂-SiC-TiC ultrahigh temperature ceramic composite, *J. Alloys Compd.* 850 (2021) 156668. <https://doi.org/10.1016/j.jallcom.2020.156668>.
- [24] N.J. Rathod, M.K. Chopra, U.S. Vidhate, N.B. Gurule, U.V. Saindane, Investigation on the turning process parameters for tool life and production time using Taguchi analysis, *Mater. Today Proc.* 47 (2021) 5830–5835. <https://doi.org/10.1016/j.matpr.2021.04.199>.
- [25] Y. Achenani, M. Saâdaoui, A. Cheddadi, G. Bonnefont, G. Fantozzi, Finite element modeling of spark plasma sintering: Application to the reduction of temperature inhomogeneities, case of alumina, *Mater. Des.* 116 (2017) 504–514. <https://doi.org/10.1016/j.matdes.2016.12.054>.
- [26] C. Wang, L. Cheng, Z. Zhao, FEM analysis of the temperature and stress distribution in spark plasma sintering: Modelling and experimental validation, *Comput. Mater. Sci.* 49 (2010) 351–362. <https://doi.org/10.1016/j.commatsci.2010.05.021>.
- [27] E. Zapata-Solvas, D.D. Jayaseelan, H.T. Lin, P. Brown, W.E. Lee, Mechanical properties of ZrB₂- and HfB₂-based ultra-high temperature ceramics fabricated by spark plasma sintering, *J. Eur. Ceram. Soc.* 33 (2013) 1373–1386. <https://doi.org/10.1016/j.jeurceramsoc.2012.12.009>.
- [28] S. Mohammad Bagheri, M. Vajdi, F. Sadegh Moghanlou, M. Sakkaki, M. Mohammadi, et al., Numerical modeling of heat transfer during spark plasma sintering of titanium carbide, *Ceram. Int.* 46 (2020) 7615–7624. <https://doi.org/10.1016/j.ceramint.2019.11.262>.
- [29] Y. Ai, Y. Yan, G. Dong, S. Han, Investigation of microstructure evolution process in circular shaped oscillating laser welding of Inconel 718 superalloy, *Int. J. Heat Mass Transf.* 216 (2023) 124522. <https://doi.org/10.1016/j.ijheatmasstransfer.2023.124522>.
- [30] C. Manière, A. Pavia, L. Durand, G. Chevallier, K. Afanga, C. Estournès, Finite-element modeling of the electro-thermal contacts in the spark plasma sintering process, *J. Eur. Ceram. Soc.* 36 (2016) 741–748. <https://doi.org/10.1016/j.jeurceramsoc.2015.10.033>.
- [31] S. Savani, M. Alipour, A. Sharma, D. Benny Karunakar, Microwave sintering of ZrB₂-based ceramics: A review, *Synth. Sinter.* 3 (2023) 143–152. <https://doi.org/10.53063/synsint.2023.33129>.
- [32] S.K. Kashyap, R. Mitra, Densification behavior involving creep during spark plasma sintering of ZrB₂-SiC based ultra-high temperature ceramic composites, *Ceram. Int.* 46 (2020) 5028–5036. <https://doi.org/10.1016/j.ceramint.2019.10.246>.
- [33] A. Shima, M. Kazemi, Influence of TiN addition on densification behavior and mechanical properties of ZrB₂ ceramics, *Synth. Sinter.* 3 (2023) 46–53. <https://doi.org/10.53063/synsint.2023.31133>.
- [34] T.R. Paul, M.K. Mondal, M. Mallik, Densification behavior of ZrB₂-MoSi₂-SiCw composite processed by multi stage spark plasma sintering, *Ceram. Int.* 47 (2021) 31948–31972. <https://doi.org/10.1016/j.ceramint.2021.08.081>.
- [35] M. Patel, V. Singh, J.J. Reddy, V.V. Bhanu Prasad, V. Jayaram, Densification mechanisms during hot pressing of ZrB₂-20vol.% SiC composite, *Scr. Mater.* 69 (2013) 370–373. <https://doi.org/10.1016/j.scriptamat.2013.05.021>.
- [36] M. Shahedi Asl, M. Ghassemi Kakroudi, Fractographical assessment of densification mechanisms in hot pressed ZrB₂-SiC composites, *Ceram. Int.* 40 (2014) 15273–15281. <https://doi.org/10.1016/j.ceramint.2014.07.023>.